CFD-based geometrical shape optimization of a packed-bed reactor combining multi-objective and adjoint system methods

Alexis Courtais, François Lesage, Yannick Privat, Cyril Pelaingre, Abderrazak M Latifi

CFD-based geometrical shape optimization of a packed-bed reactor combining multi-objective and adjoint system methods

Alexis Courtais[1], François Lesage[1], Yannick Privat[2,3], Cyril Pelaingre[4], and Abderrazak M. Latifi[1,*]

[1]Laboratoire Réactions et Génie des Procédés, CNRS-ENSIC, Université de Lorraine, 1 rue de Grandville, BP20451, 54001, Nancy Cedex, France
[2]Institut de Recherche Mathématique Avancée, CNRS, Université de Strasbourg, 7 rue René-Descartes, 67084, Strasbourg Cedex, France
[3]Institut Universitaire de France (IUF)
[4]Centre Européen de Prototypage et Outillage Rapide, CIRTES, 29 bis voie de l'innovation, 88100 Saint-Dié-des-Vosges, France
[*]abderrazak.latifi@univ-lorraine.fr

Abstract

This paper presents the development of a geometric shape optimization methodology based on the so-called "Hadamard boundary variation" method for performing very general domain deformations, and the related concept of domain differentiation. The resulting method is used to determine the optimal configuration of a two-dimensional packed-bed reactor that simultaneously optimizes its conversion rate and fluid energy dissipation, and where a homogeneous first-order reaction or a catalytic surface reaction takes place. The considered multi-objective optimization problem is subjected to four constraints: the process model constraints consisting of the Navier-Stokes, continuity and mass balance equations, an iso-volume and two manufacturing constraints. The approach to solve the problem is based on the linear scalarization method which converts the multi-objective problem into a single objective problem. The adjoint system method is used to compute the gradient of the performance indices and constraints. Since the indices are conflicting, the solution of the problem is a set of solutions, called *Pareto front*. Each optimal solution is evaluated using multi-attribute utility theory (MAUT) to determine the best optimal shape of the reactor. Finally, the resulting shape is fabricated using a 3D printing technique and will be experimentally validated.

Keywords: Multi-objective shape optimization, Adjoint system method, OpenFOAM environment, Packed-bed reactor, Additive manufacturing, Multi-criteria decision-making

1 Introduction

Fixed-bed reactors are important in process engineering since they are among the most common reactors in the chemical industry. Indeed, they are used in catalytic hydrogenation (Logunova and Chernyak, 2007), hydrotreatment and hydrocracking of oil fractions (Delmon et al., 1997), power-to-gas techniques (Bremer et al., 2017), wastewater treatment (Ramaswami et al., 2019), etc. Despite their wide use, their design still poses many problems due to the complex phenomena involved and the lack of reliable and accurate data on hydrodynamics and transfer phenomena, especially at the local scale. Nowadays, the shape of fixed-bed reactors involved in a process is predefined (structured or random packing) and the process is optimized by its operating conditions (inlet concentrations, flow rate, temperature, etc.). Although optimal with respect to these decision variables, the reactor may exhibit non-ideal behaviors such as stagnation or channeling zones that reduce its efficiency and even its lifetime. It is therefore important to overcome these effects by modifying the shape of the device and shape optimization techniques are well suited to address these issues.

In the context of packed-bed reactors, the objective of shape optimization is to determine the packing configuration that optimizes one or more criteria while satisfying operational and manufacturing constraints. Shape optimization techniques can be classified into three main categories, depending on the degree of freedom and complexity of the algorithm (Allaire and Schoenauer, 2007): (a) parameter optimization, (b) geometry optimization, and (c) topology optimization. The approach developed in this work is an iterative geometry optimization method which allows us to test a wide range of possible shapes but prevents topology changes, i.e., creation or disappearance of inclusions in two dimensions (Allaire and Schoenauer, 2007). It is a gradient based method which computes the so-called shape gradient of the performance index and the constraints by means of the adjoint system method. In this respect, geometry optimization methods offer an appropriate compromise between the advantages and disadvantages of other categories of shape optimization. They allow large and sufficient modifications of the shape (in contrast to parametric methods) and therefore considerably improve the performance of the object while avoiding high CPU consumption. Finally, they guarantee the manufacturability of the final object (Courtais et al., 2021b) since its topology is chosen by the user (unlike topological methods).

In process engineering, shape optimization methods are not widely deployed, in comparison to other fields such as mechanical engineering, where structural optimization has been intensively investigated in the last decade (Allaire et al., 2017; Feppon et al., 2020; Sun et al., 2019). In addition, shape optimization methods used so far in process engineering dealt with systems involving fluid flow and heat transfer phenomena. (Henrot and Privat, 2010; Hadad et al., 2020; Joo et al., 2017). In contrast, systems involving mass transfer such as reactors have not been the subject of extensive studies. Obviously, several studies have already applied shape optimization techniques to determine optimal reactor shapes (Grundtvig et al., 2017; Hoseini et al., 2020). However, the improvements in reactor performance are not maximal due to the limiting nature of the parameter optimization methods used.

Furthermore, in most process engineering studies, the investigated problem is formulated as a single-objective minimization or maximization problem (e.g. the reactant concentration at the reactor outlet (Courtais et al., 2021b) or the average outlet fluid temperature (Feppon et al., 2021)) under constraints imposed by the optimized process. However, the constant improvement of the industrial sector frequently requires to consider and optimize simultaneously multiple conflicting objectives (e.g. the pressure drops and the heat transfer rate for a heat exchanger (Bianco et al., 2021)). The solution of the resulting problem is no longer a single solution but a whole set of optimal solutions called Pareto front. The solution of this kind of problems requires the use of multi-objective optimization techniques (Collette and Siarry, 2004).

The shape optimization approach developed in this paper is based on the Hadamard boundary variation method which is used in order to determine the packing structure of a packed-bed reactor where a homogeneous first order reaction or a catalytic surface reaction takes place. The problem studied is formulated as a multi-objective optimization problem involving two conflicting objective functions (Courtais et al., 2021a,b): the energy dissipation in the fluid and the average concentration of reactant at the reactor outlet. For example, an increase in energy dissipation, e.g. pressure drop, would probably be correlated with a better mixing, which would have positive influence on conversion, but will have a negative economic impact.

The admissible shapes of the optimization problem are subjected to two thickness constraints accounting for the manufacturability properties of the optimal reactors, an iso-volume constraint and the process model described by a system of Navier-Stokes and convection-diffusion equations. The developed methodology is implemented and solved within the OpenFOAM CFD software to estimate the Pareto front and the selected optimal shape is chosen using the multi-attribute utility theory (MAUT, (Keeney et al., 1979)) according to the preferences of the decision-maker.

Although this study cannot be used directly to optimize an actual, industrial scale reactor, the methodology described could be applied to such systems provided the optimization problem can be formulated. Nonetheless, this formulation might be not obvious: taking into account a turbulent flow, for example, requires formulating and solving the corresponding adjoint equations, which is still an issue for Reynolds stress models.

The purpose of this paper is mostly to present this methodology.

The article is organized as follows. The investigated multi-objective optimization problem is first described in Section 2. Section 3 is devoted to the presentation of the mathematical methods used to solve the problem, it describes in particular the multi-objective optimization approach, the shape optimization method and the multiple-criteria decision analysis. The resulting numerical results are gathered in Section 4, as well as the manufacturing of the selected optimal shape of the reactor. Finally, Section 5 provides a conclusion to this work and some perspectives for future studies.

2 Formulation of the multi-objective shape optimization problems

2.1 Governing equations

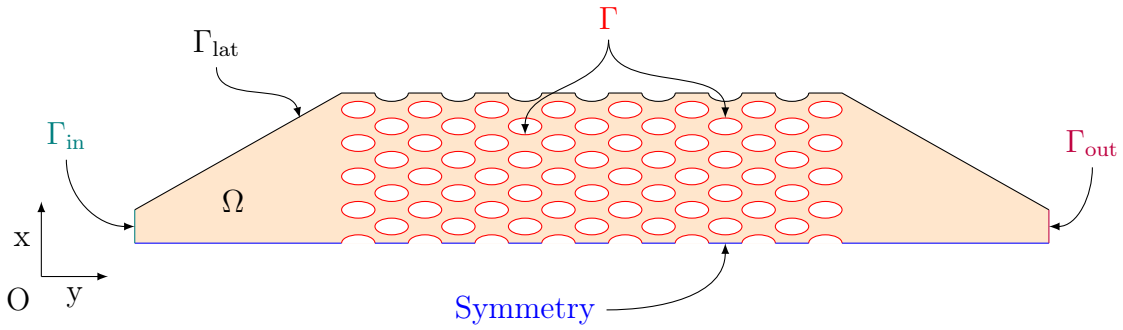

Figure 1: Reactor geometry used as the initial shape Ω_0 for the optimization process. The boundary condition of symmetry is applied on the axis located in the center of the reactor.

The initial configuration of the considered reactor consists of a two-dimensional packed-bed reactor in which 128 cylindrical obstacles are staggered with longitudinal and transverse rows of 1 cm each. A schematic representation of this structured reactor is displayed in Fig. 1. The studied domain corresponding to the reactor is designated by the subset $\Omega \subset \mathbb{R}^2$ and its geometry is described by the union of its outer boundaries: the packing Γ, the lateral wall Γ_{lat}, the fluid inlet Γ_{in} and outlet Γ_{out}. The boundary Γ which coincides with the structured packing in the initial shape (Fig. 1) represents the decision variable of the optimization problem that is modified throughout the optimization procedure. It is often called the "free boundary", the others will not evolve and are named "fixed boundaries". The fluid relative pressure is imposed equal to zero at the reactor outlet, the single-phase liquid is assumed to be Newtonian and incompressible, the flow regime is supposed to be laminar and the steady state is considered to be reached. The liquid momentum transport in Ω is therefore described by the Navier-Stokes and continuity equations associated with the usual boundary conditions according to the following system of equations:

$$\begin{cases} -\nu\Delta\boldsymbol{U} + \boldsymbol{U}\cdot\nabla\boldsymbol{U} + \nabla p = 0 & \text{in } \Omega \quad (1a) \\ \nabla\cdot\boldsymbol{U} = 0 & \text{in } \Omega \quad (1b) \\ \boldsymbol{U} = \boldsymbol{U_{in}} & \text{on } \Gamma_{\text{in}} \quad (1c) \\ \boldsymbol{U} = 0 & \text{on } \Gamma_{\text{lat}} \cup \Gamma \quad (1d) \\ \boldsymbol{\sigma}(\boldsymbol{U}, p)\boldsymbol{n} = 0 & \text{on } \Gamma_{\text{out}} \quad (1e) \end{cases}$$

where ν is the fluid kinematic viscosity, $\boldsymbol{U}$ and p are the velocity and the kinematic pressure (the ratio between the absolute pressure and the density of the fluid) of the fluid and $\boldsymbol{n}$ is the outward unit normal vector to the boundary. In Eq. (1e), $\sigma(\boldsymbol{U}, p)$ denotes the viscous stress tensor given by:

$$\sigma(\boldsymbol{U}, p) = 2\nu\varepsilon(\boldsymbol{U}) - p\boldsymbol{I} \text{ with } \varepsilon(\boldsymbol{U}) = \frac{1}{2}(\nabla\boldsymbol{U} + (\nabla\boldsymbol{U})^T) \tag{2}$$

where I is the identity matrix and $\varepsilon(\boldsymbol{U})$ is the strain-rate tensor.

Since the two case studies involve different types of reactions, the convection-diffusion equations describing mass transfer in the reactor are presented separately in the following sections.

2.1.1 First case study: homogeneous reaction (HR)

The first studied case deals with a first order homogeneous reaction that takes place in the packed-bed reactor. The considered mechanism is of the type R $\rightarrow$ P and its reaction kinetics is given by:

$$r = kC \tag{3}$$

where C is the concentration of the reactant and k the kinetic rate. Moreover, it is considered that the reaction does not occur on the walls Γ and Γ_{lat}. The mass balance of the reactant is therefore described by the following convection-diffusion system of equations:

$$\begin{cases} -\mathcal{D}\Delta C + \boldsymbol{U}\cdot\nabla C + kC = 0 & \text{in } \Omega \quad (4a) \\ C = C_{\text{in}} & \text{on } \Gamma_{\text{in}} \quad (4b) \\ \dfrac{\partial C}{\partial \boldsymbol{n}} = 0 & \text{on } \Gamma_{\text{lat}} \cup \Gamma_{\text{out}} \cup \Gamma \quad (4c) \end{cases}$$

where $\mathcal{D}$ is the diffusion coefficient of the reactant. In this homogeneous reaction case, it is assumed that the packing only acts as a static mixer.

2.1.2 Second case study: surface reaction (SR)

The second studied case considers a catalytic surface reaction occurring in the reactor, and particularly on the walls Γ and Γ_{lat} considered as impregnated with catalyst. The catalytic reaction is assumed to be limited by the external mass transfer. Therefore, the reactant concentration is imposed equal to zero at the boundaries Γ and Γ_{lat} in the following system of mass balance equations:

$$\begin{cases} -\mathcal{D}\Delta C + \boldsymbol{U}\cdot\nabla C = 0 & \text{in } \Omega \quad (5a) \\ C = C_{\text{in}} & \text{on } \Gamma_{\text{in}} \quad (5b) \\ C = 0 & \text{on } \Gamma_{\text{lat}} \cup \Gamma \quad (5c) \\ \dfrac{\partial C}{\partial \boldsymbol{n}} = 0 & \text{on } \Gamma_{\text{out}} \quad (5d) \end{cases}$$

It is important to point out that the volume reaction term kC in Eq. (4a) does no longer appear in Eq. (5a) since it is assumed that the reaction only occurs on the walls.

2.2 Optimization problems description

2.2.1 Performance indices

The two (conflicting) objectives considered are the energy dissipation due to viscous fluid friction J_1 and the average reactant concentration at the outlet boundary J_2. They are expressed by the following relations Courtais et al. (2021b):

$$J_1(\Omega) = 2\nu \int_\Omega |\varepsilon(\boldsymbol{U})|^2 \, dx \tag{6}$$

$$J_2(\Omega) = \int_{\Gamma_{\text{out}}} C \, d\sigma \tag{7}$$

where $\boldsymbol{U}$ is the solution of Eqs. (1) and C is the solution of Eqs. (4) or (5) depending on the considered case. In Eq. (6), the integrant term is $|\varepsilon(\boldsymbol{U})|^2 = \varepsilon(\boldsymbol{U}) : \varepsilon(\boldsymbol{U})$ where the notation ":" represents the Frobenius inner product of two matrices 3×3 with real coefficients, defined by $A : B = \sum_{i,j=1}^{3} A_{ij} B_{ij}$ (Hjørungnes, 2011). For practical purposes, minimizing those two objectives is relevant since the pressure losses and the conversion rate of the reactor are functions of these criteria. Thus, minimizing J_1 and J_2 simultaneously leads to maximizing the conversion rate while minimizing the pressure drop in the packed-bed reactor.

2.2.2 Decision variables

The decision variables of the multi-objective optimization problem are the shape and the positions of each obstacle (i.e. the packing Γ).

2.2.3 Set of constraints

The optimization problem is subjected to the following four constraints:

- The process model equations which consist of momentum, continuity and mass balance equations. They are described in detail in Section 2.1.
- In order to compare the initial and optimal shapes of the reactor, the residence time is kept the same in both shapes. To do this, the volume of the reactor is prescribed equal to that of the initial reactor according to the following iso-volume constraint:

$$C_{\mathcal{V}}(\Omega) = \mathcal{V}(\Omega) - \mathcal{V}(\Omega_0) = 0 \tag{8}$$

  where $\mathcal{V}(\Omega_0)$ and $\mathcal{V}(\Omega)$ stand for the volume of the initial and optimal reactors respectively. Since the flow rate is not modified during the optimization process, imposing an iso-volume constraint is equivalent to maintaining the residence time constant.

- The Stratoconception manufacturing process (Barlier, 1991) is used to print in 3D the reactors. It involves standard manufacturing of thin layers that are subsequently stacked and assembled. This implies a minimum obstacle thickness and a minimum distance between them (i.e. the pores width), leading to the following two inequality constraints:

$$d^{\text{obs}} > d^{\text{obs}}_{\text{min}} \qquad \text{and} \qquad d^{\text{pore}} > d^{\text{pore}}_{\text{min}} \tag{9}$$

where d^{obs} and d^{pore} are the obstacles thickness and the pore width (Fig. 2), $d^{\text{obs}}_{\text{min}}$ and $d^{\text{pore}}_{\text{min}}$ are the corresponding lower bounds.

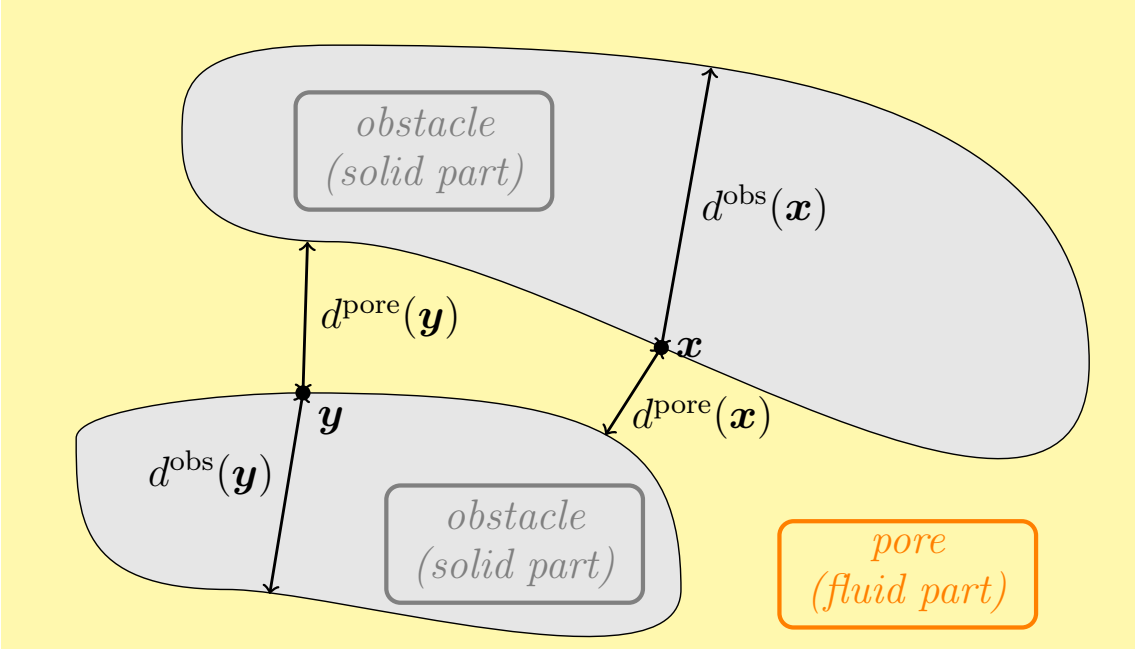

Figure 2: Schematic illustration of the thickness of obstacles and of the distance between them.

These two constraints are pointwise, i.e. they are in fact defined at each point of the boundary $\partial\Omega$. From a practical point of view, once discretized, each constraint turns into $2N$ inequalities, where N denotes the number of boundary points. Moreover, they both involve constraints on minimum distances between the two sides of an obstacle or between two obstacles, which raises mathematical and practical difficulties since they are not differentiable in the sense of Hadamard (Feppon et al., 2020). Hence, such constraints must be reformulated (e.g. as penalty functions Allaire et al. (2016)) or processed differently from the usual treatment (i.e. by aggregation within the Lagrangian functional). The methodology adopted is detailed in Courtais et al. (2021b).

2.2.4 Problem formulation

The shape optimization problems subjected to the process model equations, manufacturing and iso-volume constraints investigated in this work are then formulated as:

$$\begin{aligned} \underset{\Omega}{\text{Pareto-min}} \quad & [J_1(\Omega); J_2(\Omega)]^T \\ \text{s.t.} \quad & \Omega \in \mathcal{C} \\ & \text{Eqs. (1)-(2)-(4) or (1)-(2)-(5)} \end{aligned} \tag{$\mathcal{P}_1$}$$

where $\mathcal{C}$ represents the set of reactor shapes meeting the iso-volume and manufacturing constraints:

$$\mathcal{C} = \{\Omega \subset \mathbb{R}^2 \mid C_{\mathcal{V}}(\Omega) = 0,\ d^{\text{obs}} > d^{\text{obs}}_{\text{min}} \ \text{ and } \ d^{\text{pore}} > d^{\text{pore}}_{\text{min}}\}. \tag{10}$$

The wording "Pareto-min" above means that optimality for these problems refers to the notion of *Pareto optimality*.

The solution of a multi-objective optimization problem of two conflicting objectives J_1 and J_2 is called Pareto front. It is defined as the set of pairs (J_1^*, J_2^*) of optimal values for the problem of minimizing any convex combination of J_1 and J_2. Note that, when dealing with more objectives, the definition of Pareto front is more intricate and involves tools from Game theory. In section 4, we will plot the Pareto front associated with each problem considered and discuss its interpretation in terms of process engineering.

3 Mathematical methods used for problem solving

3.1 Multi-objective optimization approach

Multi-objective optimization methods may be classified in 2 main categories (Collette and Siarry, 2004): the meta-heuristic methods (e.g. Non dominated Sorting Genetic Algorithm, Multiple Objectives Genetic Algorithm, etc..) whose algorithms are based on Pareto domination and the scalar methods which reformulate the multi-objective optimization problem as a single-objective problem. Since the decision variable is the shape of the packing Γ described by about 9,000 to 16,000 boundary points, a meta-heuristic method would be CPU intensive. Therefore, a scalar method is considered. It is a linear scalarization method which aggregates the objectives as follows:

$$\begin{aligned} J(\Omega) &= \tau J_1(\Omega) + K_{\text{crit}}(1-\tau) J_2(\Omega) \\ &= \tau 2\nu \int_\Omega |\varepsilon(\boldsymbol{U})|^2 \, dx + K_{\text{crit}}(1-\tau) \int_{\Gamma_{\text{out}}} C \, d\sigma \end{aligned} \tag{11}$$

where $\tau \in [0,1]$ and $K_{\text{crit}} > 0$ is a constant ensuring the same order of magnitude of the objectives. The multi-objective optimization problem ($\mathcal{P}_1$) is therefore reformulated as the following single-objective optimization problem which is solved several times modifying the parameter τ in order to estimate the Pareto front:

$$\begin{aligned} \min_{\Omega} \quad & J(\Omega) = \tau J_1(\Omega) + K_{\text{crit}}(1-\tau) J_2(\Omega) \\ \text{s.t.} \quad & \Omega \in \mathcal{C} \\ & \text{Eqs. (1)-(2)-(4) or (1)-(2)-(5)} \end{aligned} \tag{$\mathcal{P}_2$}$$

Finally, the Lagrangian of the problem ($\mathcal{P}_2$) which combines the objectives and the volume constraint is expressed as follows:

$$\mathcal{L}(\Omega, \lambda_{\mathcal{V}}) = \tau J_1(\Omega) + K_{\text{crit}}(1-\tau) J_2(\Omega) + \lambda_{\mathcal{V}} C_{\mathcal{V}}(\Omega) \tag{12}$$

where $\lambda_{\mathcal{V}}$ is the Lagrange multiplier associated to the iso-volume constraint.

The developed mathematical approach used to solve the problem ($\mathcal{P}_2$) is based on the concept of differentiation with respect to the domain. It is detailed in Courtais (2021) and Courtais et al. (2021b) and a brief summary is provided in appendix A. The associated methodology of shape optimization is implemented within the open-source software OpenFOAM which solves the PDEs by means of finite volumes method and C++ programming language. The iterations of the algorithm are linked to each other using the "pyFoam" library, and for each iteration, the algorithm runs through a 6-step procedure which is explained in details in Courtais et al. (2021b).

3.2 Multi-criteria decision-making method

Once the estimate of the Pareto front has been determined, it is necessary to select the best reactor shape to manufacture. To this end, the optimal shapes are ranked according to the preferences of the decision-maker (i.e. how much importance is given to each objective) which are often subjective and depend on the considered process. At this stage, the concept of Pareto optimality is no longer relevant since each optimal pair (J_1^*, J_2^*) cannot be directly compared to another. Therefore, another approach must be used to rank the solutions and a multi-criteria decision analysis (MDCA) procedure is carried out using the multi-attribute utility theory (MAUT) introduced by Keeney et al. (1979). The MAUT method allows to classify the Pareto solutions in two steps:

(i) The decision-maker assigns to both criteria J_i an individual utility function u_i which evaluates the performance of a solution $\boldsymbol{x}$ in the i-th objective. The form of the selected utility function is chosen by the decision-maker but it must be monotonic and continuous (Olson, 1997). According to the literature works, three main forms are identified: exponential (Kim and Song, 2009), linear (Voola and Vinaya Babu, 2017), and power (Fonseca et al., 2020; Benyahia et al., 2011) forms. The latter form has been chosen in this work, and the individual utility functions are expressed as follows:

$$u_i(\boldsymbol{x}) = \left(\frac{J_i^{\max} - J_i(\boldsymbol{x})}{J_i^{\max} - J_i^{\min}} \right)^{\alpha_i} \tag{13}$$

where $J_i^{\max}$ and $J_i^{\min}$ are maximum and minimum values reached by objective i among the Pareto solutions. In Eq. (13), parameter α_i represents the relative tolerance factor with respect to objective i. Figure 3 illustrates the influence of the parameter α_i: for small values of the parameter α_i (e.g. $\alpha_i = 0.2$), the individual utility function u_i is less sensitive to the degradation of the associated performance index J_i in the vicinity of its optimal value. The opposite behavior of u_i occurs for large values of α_i (e.g. $\alpha_i = 5$).

(ii) The individual utility functions are then combined defining the multi-attribute utility function which allows to rate the Pareto solutions. It reads:

$$U(\boldsymbol{x}) = w u_1(\boldsymbol{x}) + (1 - w) u_2(\boldsymbol{x}) \tag{14}$$

where $w \in [0, 1]$ and $(1 - w)$ are weighting factors for each utility function to assign relative importance to either objectives.

In conclusion, the decision-maker preferences are reflected through the chosen values of w, α_1 and α_2 (see Fig. 3).

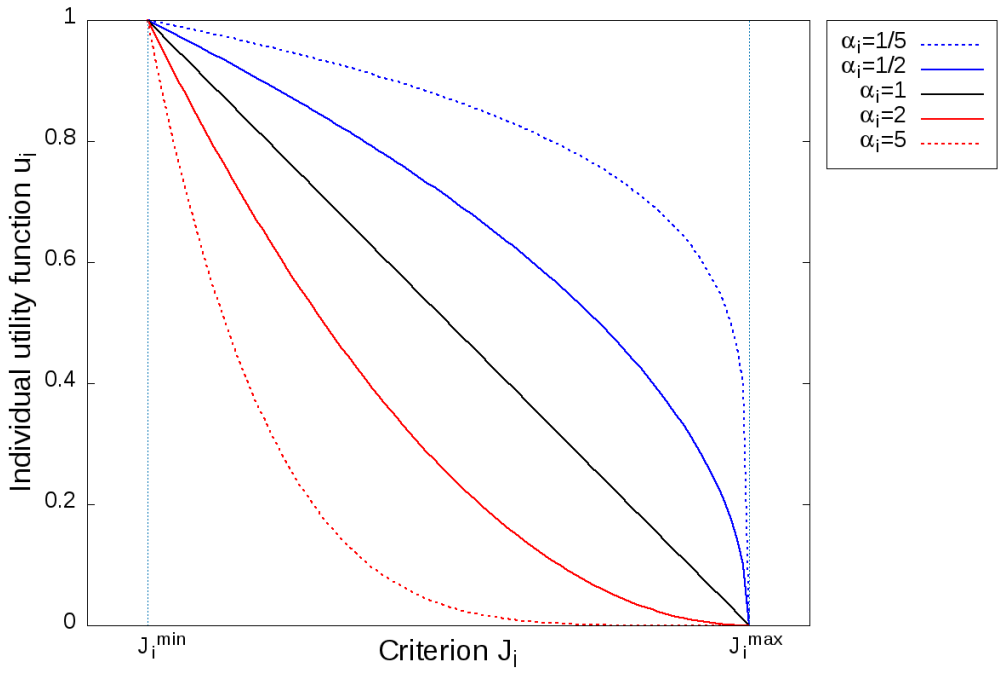

Figure 3: Influence of the relative tolerance α_i ($i = 1$ or $i = 2$) on the individual utility function.

4 Results and discussions

4.1 Numerical results

The optimization results of the two cases HR and SR are presented and discussed. The values of the parameters used are reported in Table 1 for both cases. This section is split into two parts, the first one is devoted to the optimization of the reactors where the homogeneous reaction takes place, whereas the second one presents the optimization of the reactor where the catalytic surface reaction occurs.

Table 1: Values of the parameters used in simulation and optimization.

Parameters	Values		Units	Equations
	HR case	SR case		
ν	10^{-6}	10^{-6}	$\mathrm{m}^2.\mathrm{s}^{-1}$	(1a), (26), (25) and (28)
U_{in}	10^{-2}	10^{-2}	$\mathrm{m.s}^{-1}$	(1c)
$\mathcal{D}$	10^{-9}	10^{-9}	$\mathrm{m}^2.\mathrm{s}^{-1}$	(25), (27a), (28) and (29a)
k	10^{-2}	-	s^{-1}	(4a)
γ	10^{-4}	10^{-4}	m^{-2}	(24a) and (24c)
K_{BC}	3×10^{-3}	3×10^{-3}	$\mathrm{mol.m}^{-2}.\mathrm{s}^{-1}$	(25), (28) and (26d)
K_{crit}	3×10^{-5}	3×10^{-5}	$\mathrm{m}^6.\mathrm{s}^{-3}.\mathrm{mol}^{-1}$	(12), (25) and (28)
t	10^{-1}	1.5×10^{-1}	-	(16)
$\lambda_{\mathcal{V}}^0$	0	0	-	(25) and (28)

4.1.1 Case of the homogeneous reaction

The solution of the first optimization problem (i.e. the HR case) is computed in two steps:

1. As explained in Section 3.1, the multi-objective problem ($\mathcal{P}_1$) is first recast as a single objective problem ($\mathcal{P}_2$) by aggregating the objectives into a unique performance index and by introducing a parameter $\tau \in [0:1]$.

2. Problem ($\mathcal{P}_2$) is then solved several times (25 times in this case) by modifying the parameter τ between its bounds. For each single objective resolution, the configuration displayed in Fig. 1 is used as the initial shape of the reactor.

The Pareto front obtained is presented in Fig. 4 where each solution is represented by a circle. This Pareto front emphasizes the importance of performing a multi-objective optimization in this case. Indeed, the performances of the shape optimized by Courtais et al. (2021b) using a single-objective method are displayed in Fig. 4 (green triangle), and the Pareto front is almost vertical from this point to values of J_1 around 4×10^{-12}. This shows that the energy dissipation can be reduced by about 33% at the cost of a negligible loss in conversion rate.

Optimization problems involving only one criterion (i.e. for $\tau = 0$ and $\tau = 1$) allow to compute minimal bounds of each objective; the lower bound for the energy objective is

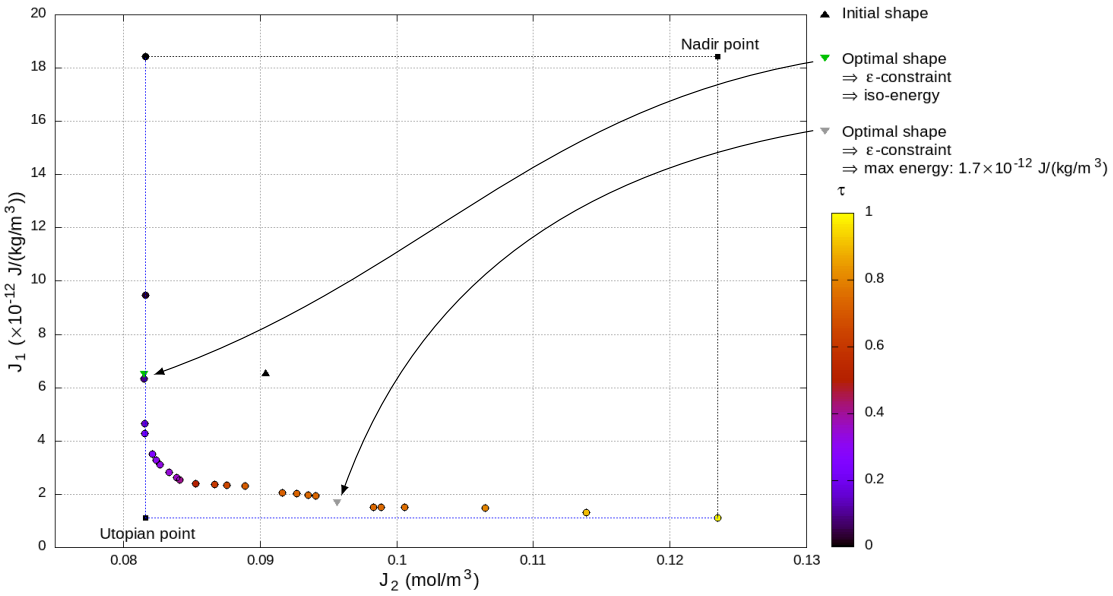

Figure 4: Pareto front of the HR case.

1.12×10^{-12} J/(kg/m^3), while it is 8.16×10^{-2} mol.m^{-3} for the conversion rate objective. Thus, it results in an utopian point whose coordinates are $(8.16 \times 10^{-2}\ ;\ 1.12 \times 10^{-12})$ which does not meet the constraints $\mathcal{C}$, and therefore, its associated configuration is not manufacturable or not suitable for practical purposes. We also define the nadir point whose coordinates are the worst values reached by the criteria within the Pareto front, i.e. $(1.24 \times 10^{-1}\ ;\ 1.84 \times 10^{-11})$. The determination of these two points will be useful thereafter, especially when choosing the best shape using the MAUT method.

Figure 5 presents the concentration and velocity profiles of the initial and different optimized reactors depending on the values of the parameter τ. For initial shape, a dead zone can be observed close to the entrance, with very low velocities (left column) leading to an almost non-reacting volume with very low concentrations (right column)

When only the criterion J_2 is optimized (i.e. $\tau = 0$), this dead zone disappears and the fluid flow in the reactor becomes homogeneous, which allows a 10-percent decrease of the criterion, and therefore, an improvement of 2.7% of the conversion rate (74.2% versus 71.5%). As highlighted in Courtais et al. (2021b), the conversion rate of this optimized reactor is very close to the one of the ideal plug flow reactor whose conversion rate is 74.6%. Consequently, in this case, the optimization procedure allows to reduce the deviation from the ideal reactor by modifying the packing structure. However, this modification leads to an increase in the energy dissipation since the reactor exhibits areas with high velocity gradients (i.e. where the channels are narrow and the velocity is high). This result was expected since the dissipated energy does not influence the performance index when the parameter τ is zero. When the values of τ increase up to 0.2, the flow remains homogeneous which leads to a negligible deterioration of the conversion rate. Nevertheless, the channels

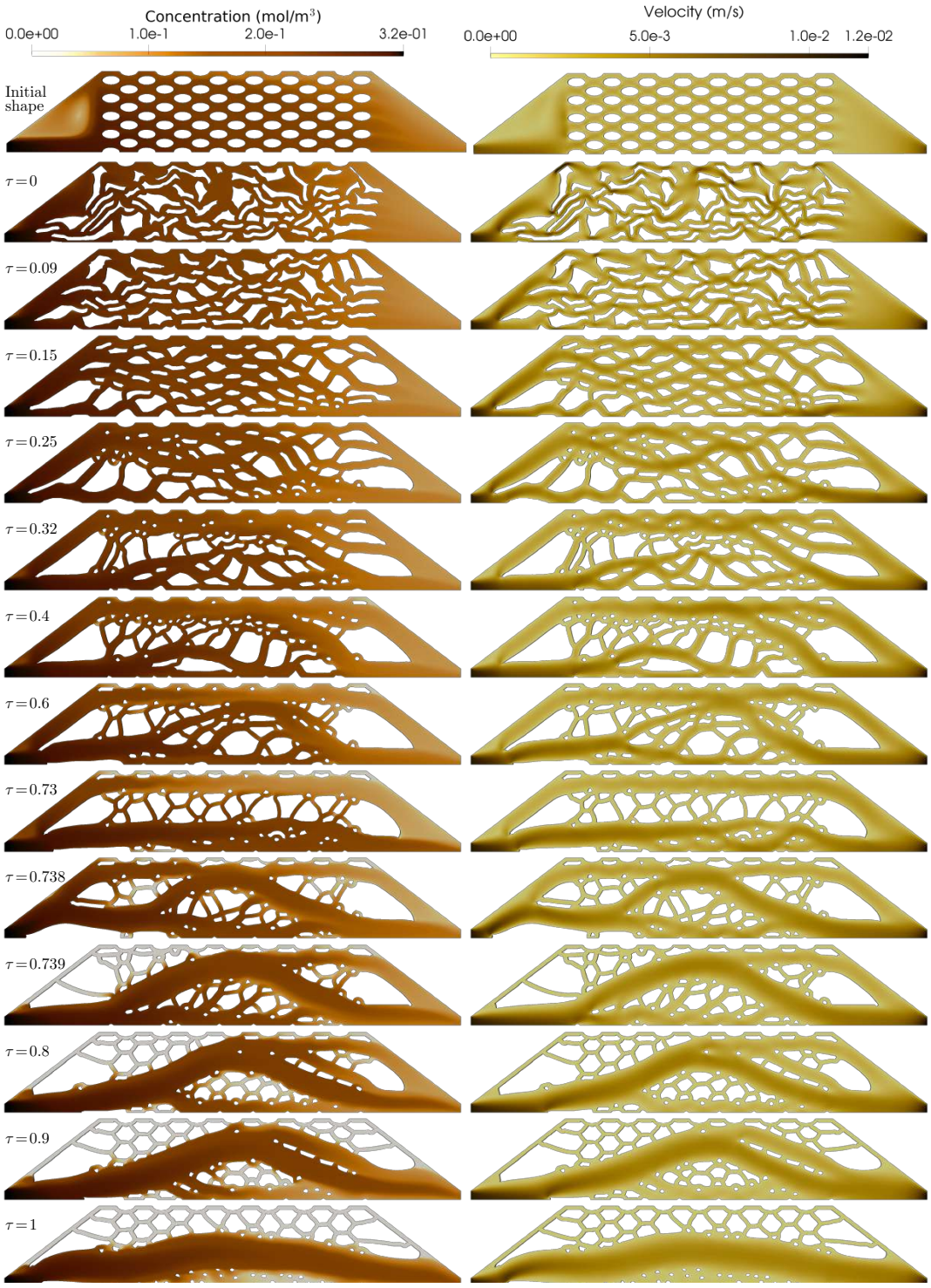

Figure 5: Concentration (left) and velocity (right) profiles in the initial (top row) and different optimized shapes – HR case.

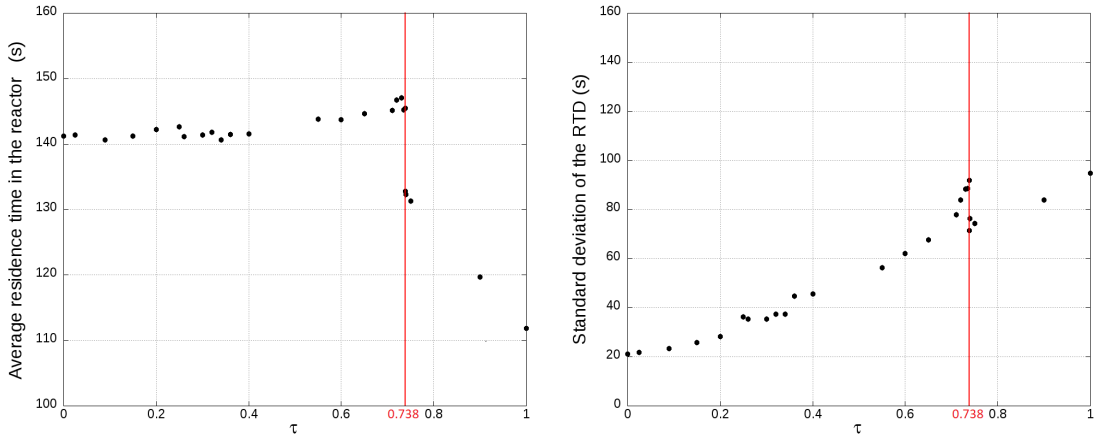

(a) Average residence time.

(b) Standard deviation of the RTDs.

Figure 6: Evolution of (a) the average residence time, and (b) the standard deviation of the RTDs as a function of τ.

width increases which reduces the velocity gradients, and therefore, the dissipated energy. On the other hand, Fig. 5 shows that the higher the weight τ, the larger the channels which ensures a decrease of the energy dissipation. However, it leads to a deterioration of the flow homogeneity, and consequently, to a reduction of the conversion rate. Moreover, when τ is close to 1 ($\tau \in [0.739 : 1]$), dead zones appear which significantly decrease the conversion rate since the reactant concentration is almost zero in these regions. Finally, for $\tau = 1$, the performance index only depends on the energy dissipation. Therefore, the reactor looks like a large channel ensuring low velocity gradients but also low conversion rate. Thus, this configuration leads to a reduction of the dissipated energy by a factor of 5.6, but the conversion rate is degraded by 9.2% (62.3% versus 71.5%).

The numerical residence time distribution of the 25 optimal reactors have been determined and are analyzed using the method of moments which consists in computing the three first order moments according to the following formula (Levenspiel, 1999):

$$\mu_i = \int_0^\infty t^i E(t) dt \tag{15}$$

where $E(t)$ is the RTD function and $i \in [0 : 2]$ is the moment order. The zeroth order is equal to one, the first order μ_1 represents the average residence time in the reactor and the second order allows to compute the standard deviation given by $\sigma = \sqrt{\mu_2 - \mu_1^2}$. The latter quantifies the homogeneity of the fluid flow in the reactor. Figure 6 presents the evolution of the average residence time and the standard deviation of RTDs versus τ. It particularly highlights the presence of dead zones in optimal reactors for $\tau > 0.739$ (Fig. 6(a)) since the average residence time slightly varies for $\tau \leqslant 0.738$, and it strongly decreases when $\tau \geqslant 0.739$ (Villermaux, 1993). It also shows the degradation of the fluid flow when the parameter τ is increased, since the standard deviation of RTDs increases with τ, as can be seen in Fig. 6(b).

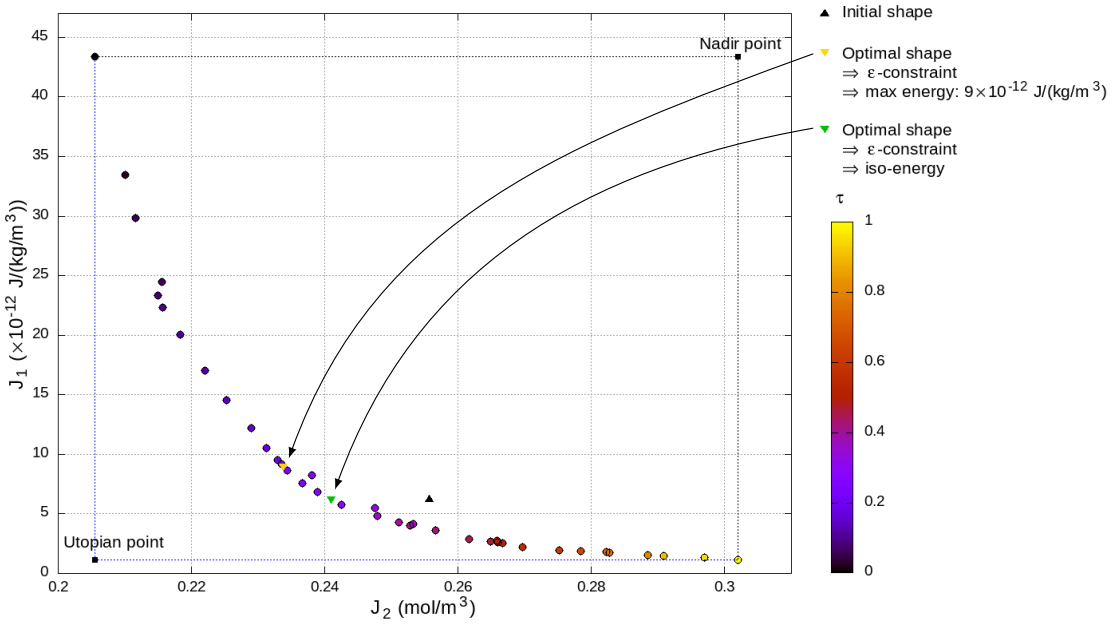

Figure 7: Pareto front of the SR case.

On the other hand, Figs 6 exhibit a discontinuity in the area near the gray diamond of the Pareto front where the optimal shapes strongly differ between $\tau \simeq 0.738$ and $\tau \simeq 0.739$ (Fig. 5). Indeed, the Pareto front seems slightly concave in this region and the linear scalarization method can only determine convex parts of Pareto fronts (Collette and Siarry, 2004). Thus, the ε-constraint method has been used in order to determine the reactor shape associated to the gray diamond displayed on Fig. 4 and whose coordinates are $(9.56 \times 10^{-2}$; $1.7 \times 10^{-12})$.

4.1.2 Case of the surface reaction

The same computation procedure is used to estimate the Pareto front made up of 40 optimal solutions determined by varying the weight τ between 0 and 1. As emphasized by Courtais et al. (2021b), a single-objective optimization requires between 7 and 10 computational days on a computer with a 3.7GHz Xeon processor. Consequently, the estimation of the whole Pareto front would be time consuming on a single computer. Thus, each single-objective optimization has been parallelized and therefore computed on 40 different nodes of the University of Lorraine supercomputer named EXPLOR.

The resulting Pareto front is displayed on Fig. 7 and a part of the optimized configurations is presented on Fig. 8. Similarly to the previous case, the optimizations involving only one criterion allow to define the utopian point $(2.06 \times 10^{-1}$; $1.12 \times 10^{-12})$ and the nadir point $(3.02 \times 10^{-1}$; $4.34 \times 10^{-11})$. The analysis of the reactor shapes displayed on Fig. 8 shows that the reactive surface increases significantly (up to 80%) between the initial and the optimized shape for $\tau = 0$, which mainly explains the improvement of the

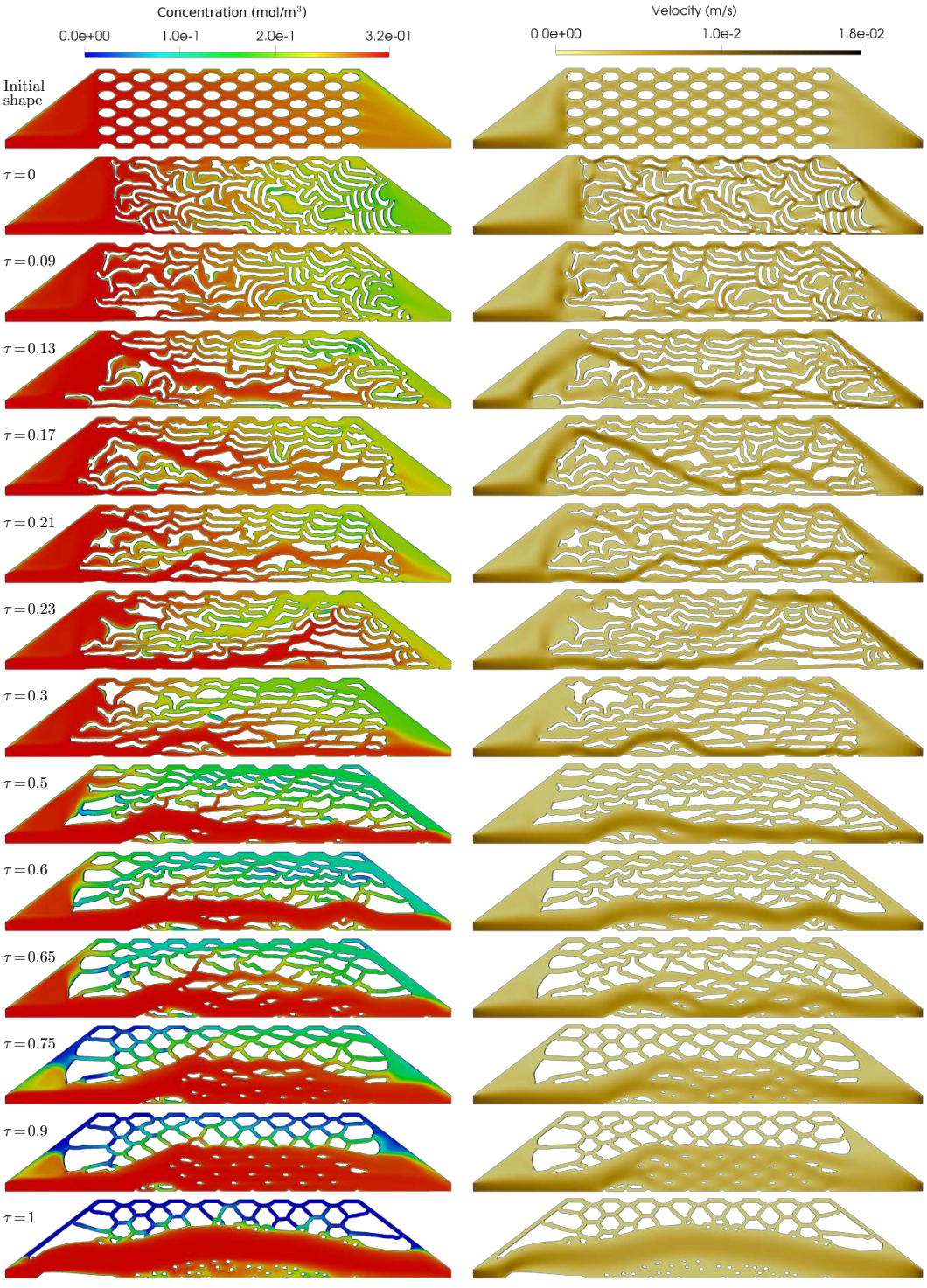

Figure 8: Concentration (left) and velocity (right) profiles in the initial (top row) and different optimized shapes – SR case.

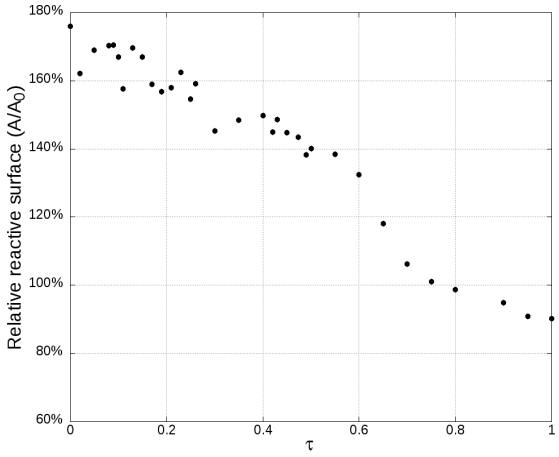

Figure 9: Evolution of the relative reactive surface area A/A_0 with τ.

conversion rate of the reactor by 16% (35.6% versus 19.6%). This improvement is also due to a good fluid flow homogeneity. However, the reactor exhibits areas with high velocity gradients leading to significant increase in energy dissipation. Moreover, when increasing τ, the flow homogeneity in the reactor is degraded (for $\tau \in [0 : 0.2]$), more and more significant channelings occur (for $\tau \in [0.2 : 0.7]$), and finally stagnation zones where the reactant concentration reaches almost zero appear (for $\tau \in [0.75 : 1]$). These three phenomena explain the deterioration of the conversion criterion when increasing the weight τ while the energy losses in the reactor are reduced. Finally, for $\tau = 1$, the optimized shape depends only on the hydrodynamics as in the previous case, the optimal reactor is therefore identical to the one presented in sub-section 4.1.1.

Figure 9 presents the evolution of the relative reactive surface area (i.e. the ratio A/A_0, A_0 being the reactive surface area of the initial shape) with τ. It particularly highlights the decrease of the reactive surface area of optimized reactors thus providing a second explanation of the deterioration of the conversion rate objective when τ is increased.

4.2 Multi-criteria decision analysis

Since the Pareto solutions are not directly comparable with each other (they are all non-dominated), the "best" optimized shape is chosen by means of a multi-criteria decision aid technique, i.e. the multi attribute utility theory (MAUT). Table 2 shows that the conversion rate (criterion J_2) is favored over the energy dissipation (criterion J_1) since the corresponding weight is higher. For both cases, the ranking of the optimized solutions is presented in Fig. 10. In this figure, the points corresponding to the higher rates are in lighter colors, and the selected solutions are highlighted by green triangles. They present the best compromise between the two conflicting objectives according to the preferences of the decision-maker.

For the HR case, the best reactor is associated to $\tau = 0.25$ and its shape has been manufactured by means of a 3D-printing technique. The manufactured shape then under-

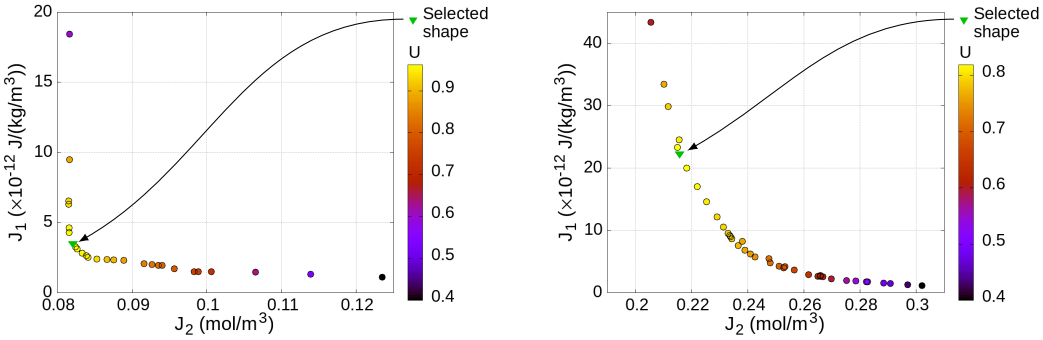

(a) HR case.

(b) SR case.

Figure 10: Multi-criteria decision analysis by means of the MAUT method - (a) HR case, (b) SR case.

Table 2: Weighting and tolerance factors assigned to each criterion.

Factor	Criterion 1	Criterion 2
w	0.4	0.6
α	0.5	1

goes tests for its experimental validation (Fig. 11) in order to validate the choice using flow and conversion experiments. The results show that the conversion rate and the dissipated energy are improved respectively by 2.6% (74.1% versus 71.5%) and by 46.7% with respect to the initial shape of the reactor. These improvements are mainly due to the good homogeneity of the flow in the reactor and to the disappearance of the dead zones . This is highlighted in Table 3 which presents the first order moment and the standard deviation of RTDs of the initial and the "best" shapes. It particularly emphasizes the disappearance of the stagnation zone in the initial shape since the average residence time (i.e. the first order moment) is higher in the "best" shape. This stagnation zone in the initial reactor is also highlighted by the standard deviation of the distributions since that associated to the initial shape is twice higher.

Table 3: Parameters of the residence time distributions (HR case)

Reactor shape	Moments of order Zero	One (mean)	Two	Standard deviation ($\sigma = \sqrt{\mu_2 - \mu_1^2}$)
Initial	1	134 s	23284 s^2	73 s
"Best"	1	142 s	21667 s^2	36 s

In the SR case, the selected shape corresponds to the weighting factor of $\tau = 0.09$ and is displayed in Fig. 8. It improves the conversion rate by 12.6% (32.2% versus 19.6%) which is mainly due to the 70-percent increase in the reactive surface of the reactor (Fig. 9), but

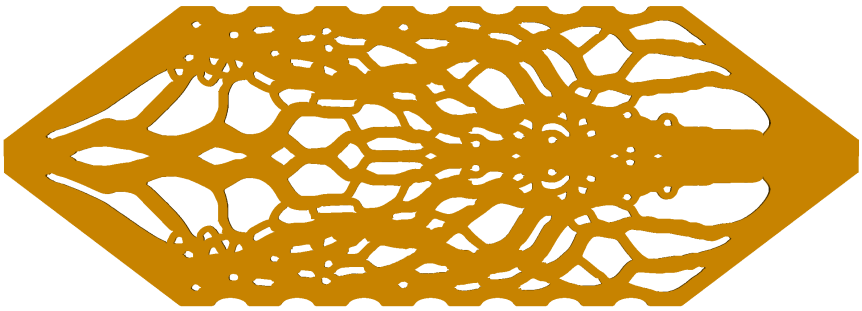

(a) Reactor configuration selected using the MAUT method.

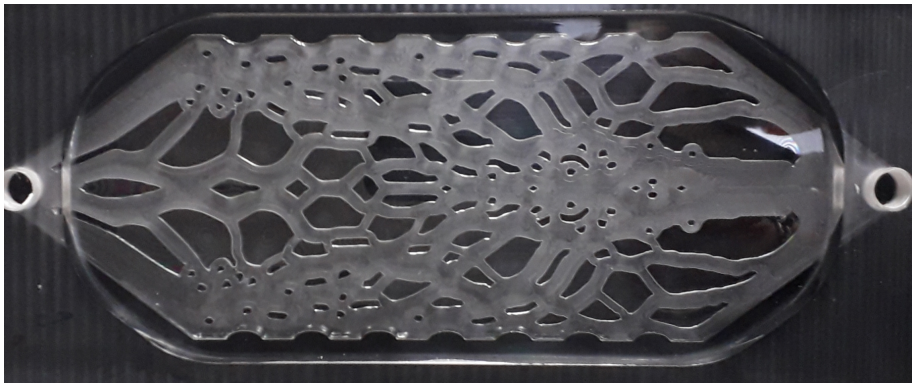

(b) Manufactured reactor.

Figure 11: Comparison between the shape selected using the MAUT method and the corresponding reactor manufactured by 3D printing.

it increases the energy loss by a factor 3.5. This choice also emphasizes the importance of carrying out multi-objective optimization since the two optimal reactors determined by Courtais et al. (2021b) with performances shown on Fig. 7 (green and yellow squares) are not the best compromises that meet the decision-maker preferences.

5 Conclusions and perspectives

A multi-objective shape optimization methodology based on the Hadamard boundary variation and adjoint system methods has been developed and implemented within OpenFOAM in order to determine the shape of a packed-bed reactor that optimizes simultaneously (i) the pressure drops and (b) the conversion rate of the reactor. For both cases, the solution of the multi-objective problem is a set of solutions and the MAUT method is used to determine the "best" shape according to the preferences of the decision-maker. The best shape has been manufactured by means of the stratoconception 3D printing method (**?**) in order to verify both the improvement of the optimal reactor performances and the accuracy of the CFD model solved at each iteration in order to compute the mesh displacement.

The developed methodology is very promising since it allows a significant improvement of the reactor performances mainly due to the ability of the geometry optimization approach to test a wide range of possible shapes. However, some elements of the methodology deserve to be improved. First, even if the developed geometry algorithm allows substantial modifications of the reactor shape unlike parametrization based algorithms, it prevents topology changes that could be relevant in those case studies, in particular for $\tau > 0.739$ in the HR case (Fig. 5). The application of a topology optimization algorithm, for instance based on the level-set (Kambampati et al., 2021) or the homogenization (Ozguc et al., 2021) methods, could constitute an interesting continuation of this work. However, its use would lead to an increase of the computational time required by an optimization procedure which already constitutes the second element that needs improvements. Indeed, one optimization procedure takes between 3 and 10 days to converge on a computer with a 3.7GHz Xeon processor depending on the case study, and the SR case has required the use of a supercomputer in order to run in parallel all single-objective computations. To reduce the CPU time, several possibilities can be investigated. Indeed, since the most CPU consuming step is the resolution of the PDEs, the use of surrogate models (Rabhi et al., 2018) that would approximate and accelerate the PDEs resolutions could be investigated. However, care should be taken since such an approach could lead to an imprecise estimate of the shape gradient.

Another point to consider is the reduction of the number of optimization iterations needed to reach convergence by using a linear search method that computes the optimal step t at each iteration. However, the computation of the optimal step is performed using a finite difference technique. Therefore, it involves several integrations of the model equations (which are PDEs – Navier-Stokes and mass balance equations) in order to compute the performance index with different values of the step (i.e. different mesh displacement). This would increase the computational effort required for each iteration, that could balance out the positive effect of the reduction of required iterations.

Finally, optimizing the reactor under its three-dimensional shape could be a natural continuation of this work.

Acknowledgment

This work was supported by the Carnot institute ICEEL. The authors are grateful for this support. The third author was also supported by the Agence Nationale de la Recherche, Project TRECOS and Project "SHAPe Optimization - SHAPO". Finally, the authors are thankful to the Mésocentre HPC EXPLOR of Université de Lorraine for the support of high performance computing.

Nomenclature

Latin symbols

C	reactant concentration	$\mathrm{mol.m^{-3}}$

$\mathcal{C}$	set of constraints of the optimization problem	-
C'	sensitivity of C with respect to the variation of Ω	$\mathrm{mol.m^{-4}}$
C_a	adjoint state of C	$\mathrm{mol.m^{-3}}$
C_{in}	reactant inlet concentration	$\mathrm{mol.m^{-3}}$
$C_{\mathcal{V}}$	iso-volume constraint	$\mathrm{m^3}$
$\mathcal{D}$	diffusion coefficient of the reactant in the solvent	$\mathrm{m^2.s^{-1}}$
$d_{\mathrm{min}}^{\mathrm{pore}}$	minimal width of pores	m
$d_{\mathrm{min}}^{\mathrm{obs}}$	minimal thickness of obstacles	m
G	shape gradient functional	-
J	aggregation of the performance indices	-
J_1	energy criterion	$\mathrm{J/(kg/m^3)}$
J_2	conversion criterion	$\mathrm{mol.m^{-3}}$
k	kinetic constant	$\mathrm{s^{-1}}$
$\mathcal{L}$	Lagrangian of the optimization problem	-
$\boldsymbol{n}$	boundary normal vector	-
p	kinematic pressure field	$\mathrm{Pa.m^3.kg^{-1}}$
p'	sensitivity of p with respect to the variation of Ω	$\mathrm{Pa.m^2.kg^{-1}}$
p_a	pressure of the adjoint state to ($\boldsymbol{U}$, p)	$\mathrm{Pa.m^3.kg^{-1}}$
s.t.	subject to	-
t	step of the optimization method	-
$\boldsymbol{U}$	fluid flow velocity	$\mathrm{m.s^{-1}}$
$\boldsymbol{U'}$	sensitivity of $\boldsymbol{U}$ with respect to the variation of Ω	$\mathrm{s^{-1}}$
$\boldsymbol{U_a}$	velocity of the adjoint state to ($\boldsymbol{U}$, p)	$\mathrm{m.s^{-1}}$
$\boldsymbol{U}_{\mathrm{in}}$	fluid velocity profile imposed at the reactor inlet	$\mathrm{m.s^{-1}}$
$\boldsymbol{V}$	vector field representing the displacement of the mesh	m
$\mathcal{V}(\Omega)$	volume of Ω	$\mathrm{m^2}$

Greek symbols

α_i	tolerance factor associated to each objective	-
γ	parameter allowing to adjust the diffusion of the mesh	$\mathrm{m^2}$
Γ	free boundary of the domain Ω	-
Γ_{in}	fluid inlet of Ω	-
Γ_{out}	fluid outlet of Ω	-
Γ_{lat}	lateral wall of Ω	-
$\partial\Omega$	union of the boundaries of Ω	-
$\lambda_{\mathcal{V}}$	Lagrange multiplier associated to the volume constraint	-
ν	fluid kinematic viscosity	$\mathrm{m^2.s^{-1}}$
τ	weighting factor	-
Ω	studied domain	-

Indices

a refer to an adjoint state

in refer to reactor inlet Ω

A Summary of the developed mathematical approach

A.1 Differentiation with respect to the domain

The shape optimization approach developed in this work is based on a gradient based iterative method: the Hadamard boundary variation method (Allaire and Schoenauer, 2007). Starting from an initial object configuration, the method computes a sequence of shapes that improve the objective at each iteration by adapting the position of the boundaries. The method relies on the concept of differentiation with respect to the domain which consists in determining the sensitivity of the Lagrangian with respect to the following perturbation of the free boundary (Henrot and Pierre, 2005):

$$\Omega_{i+1} = (\mathrm{Id} + t\boldsymbol{V})(\Omega_i) \tag{16}$$

where Id is the identity function, t is the step of the iterative method, and $\boldsymbol{V}$ is the vector field describing the mesh displacement. The small perturbation of the free boundary is therefore described by the vector $t\boldsymbol{V}$. In other words, the purpose of Hadamard's method is to determine the step t and the displacement vector field $\boldsymbol{V}$ leading to a decrease of the Lagrangian functional at each iteration. Those two variables are determined using the computation of an adjoint state, allowing to compute the gradient of the Lagrangian by introducing some adjoint system equations. In this paper, two adjoint system equations are introduced: one is associated to the fluid equations and the other is associated to the convection-diffusion equations.

In the framework of the Hadamard method, the derivative with respect to the domain of a functional in the $\boldsymbol{V}$ direction, such as the Lagrangian, is defined as follows:

$$\mathcal{L}'(\Omega, \lambda_{\mathcal{V}})(\boldsymbol{V}) = \lim_{t \to 0} \frac{\mathcal{L}(\Omega_t) - \mathcal{L}(\Omega)}{t} \tag{17}$$

where $\Omega_t = (\mathrm{Id} + t\boldsymbol{V})(\Omega)$ represents a "small" perturbation of the domain Ω. Usual differentiation formulas are applied to compute the shape derivative (or derivative with respect to the domain) of the Lagrangian functional (12), leading to

$$\mathcal{L}'(\Omega, \lambda_{\mathcal{V}})(\boldsymbol{V}) = \tau J_1'(\Omega)(\boldsymbol{V}) + K_{\mathrm{crit}}(1-\tau) J_2'(\Omega)(\boldsymbol{V}) + \lambda_{\mathcal{V}} C_{\mathcal{V}}'(\Omega)(\boldsymbol{V}) \tag{18}$$

Let us express the shape derivative of each term of Eq. (18), according to Allaire and Schoenauer (2007); Henrot and Pierre (2005):

$$J_1'(\Omega)(\boldsymbol{V}) = 2\nu \int_{\partial\Omega} |\varepsilon(\boldsymbol{U})|^2 (\boldsymbol{V} \cdot \boldsymbol{n})\, d\sigma + 4\nu \int_{\Omega} \varepsilon(\boldsymbol{U}) : \varepsilon(\boldsymbol{U'})\, dx \tag{19}$$

$$J_2'(\Omega)(\boldsymbol{V}) = \int_{\Gamma_{\mathrm{out}}} C'\, d\sigma \tag{20}$$

$$C_{\mathcal{V}}'(\Omega)(\boldsymbol{V}) = \int_{\partial\Omega} (\boldsymbol{V} \cdot \boldsymbol{n}) d\sigma \tag{21}$$

In Eqs. (19) and (20), $\boldsymbol{U'}$ and C' are respectively the sensitivities of $\boldsymbol{U}$ and C with respect to the aforementioned small perturbation of the free boundary Γ (see for example Henrot and Privat (2010); Bonnivard et al. (2018) for additional explanations). Using Eqs. (19), (20) and (21), the shape derivative of the Lagrangian functional rewrites:

$$\begin{aligned}\mathcal{L}'(\Omega,\lambda_{\mathcal{V}})(\boldsymbol{V}) =& 2\nu\tau\int_{\partial\Omega}|\varepsilon(\boldsymbol{U})|^2(\boldsymbol{V}\cdot\boldsymbol{n})\,d\sigma + 4\nu\tau\int_{\Omega}\varepsilon(\boldsymbol{U}):\varepsilon(\boldsymbol{U'})\,dx \\ &+ K_{\text{crit}}(1-\tau)\int_{\Gamma_{\text{out}}} C'\,d\sigma + \lambda_{\mathcal{V}}\int_{\partial\Omega}(\boldsymbol{V}\cdot\boldsymbol{n})d\sigma\end{aligned} \tag{22}$$

However, and for practical reasons, equation (22) is not directly applicable since some of its terms do not depend explicitly on the normal component of the deformation field $(\boldsymbol{V}\cdot\boldsymbol{n})$. Indeed, the dependence is carried out through $\boldsymbol{U'}$ and C'. In this form, choosing a suitable displacement ensuring a descent of the Lagrangian is not straightforward. The objective of the method is to reformulate the Lagrangian shape derivative under the form (Henrot and Pierre, 2005):

$$\mathcal{L}'(\Omega,\lambda_{\mathcal{V}})(\boldsymbol{V}) = \int_{\partial\Omega} G(\Omega,\lambda_{\mathcal{V}})(\boldsymbol{V}\cdot\boldsymbol{n})d\sigma \tag{23}$$

where $G(\Omega,\lambda_{\mathcal{V}})$ is the so-called shape gradient, a functional defined on the free boundary which depends on the solution of the process model ($\boldsymbol{U}$, p, and C) and the adjoint variables introduced by the method ($\boldsymbol{U_a}$, p_a, and C_a) but not on the displacement $\boldsymbol{V}$. Once an expression such as (23) is obtained, it is simple to derive a displacement field leading to a descent of the Lagrangian functional. Indeed, moving the free boundary according to $(\boldsymbol{V}\cdot\boldsymbol{n}) = -G(\Omega,\lambda_{\mathcal{V}})$ would directly imply $\mathcal{L}'(\Omega,\lambda_{\mathcal{V}})(\boldsymbol{V}) \leqslant 0$, and therefore a decrease of the Lagrangian. However, this approach to determine the displacement $\boldsymbol{V}$ is not appropriate in practice because it requires to remesh the shape at each iteration which would significantly increase the computational time. Such method is also known to generate undesired oscillations of the boundary due to the low regularity of the resulting perturbation. Indeed, since $G(\Omega,\lambda_{\mathcal{V}})$ is only defined on the free boundary, this approach determines the displacement only for the boundaries, and not for all mesh points (Allaire and Schoenauer, 2007). Consequently, we need to extend the displacement inside the mesh. For this purpose, the vector field $\boldsymbol{V}$ is computed from the shape gradient values by solving the following system of equations (Courtais, 2021; Dapogny et al., 2018):

$$\begin{cases} -\gamma\Delta\boldsymbol{V} + \boldsymbol{V} = 0 & \text{in } \Omega & \text{(24a)} \\ \boldsymbol{V} = 0 & \text{on } \Gamma_{\text{in}}\cup\Gamma_{\text{out}}\cup\Gamma_{\text{lat}} & \text{(24b)} \\ \gamma\nabla\boldsymbol{V}\boldsymbol{n} = -G(\Omega,\lambda_{\mathcal{V}},\lambda_{\mathcal{E}})\boldsymbol{n} & \text{on } \Gamma & \text{(24c)} \end{cases}$$

where $\gamma > 0$ is a parameter allowing to adapt more or less the diffusion of the mesh displacement. Once the vector field $\boldsymbol{V}$ is determined, relation (16) is applied to all mesh points in order to move the mesh for the following iteration. Finally, it only remains to establish an expression for the shape gradient functional $G(\Omega,\lambda_{\mathcal{V}})$. Since the two investigated case studies involve slightly different process model, the formulations of the shape gradient functional and the adjoint system equations are provided independently.

A.2 Homogeneous reaction case (HR case)

The calculation of the shape gradient expression is detailed in Courtais (2021). It is expressed as:

$$G(\Omega, \lambda_{\mathcal{V}}, \lambda_{\mathcal{E}}) = 2\nu(\varepsilon(\boldsymbol{U}) : \varepsilon(\boldsymbol{U_a}) - \tau\varepsilon(\boldsymbol{U}) : \varepsilon(\boldsymbol{U})) - \frac{K_{\text{crit}}}{K_{\text{BC}}}(1-\tau)\mathcal{D}C_a\Delta C + \lambda_{\mathcal{V}}, \tag{25}$$

where the parameter $K_{\text{BC}} \neq 0$ represents a constant introduced in the outlet boundary condition of the adjoint states (27) and (29) to ensure the same unit of measure of the terms of Eqs. (27d), (29c) and (25). $(\boldsymbol{U_a}, p_a)$ denotes the adjoint state to $(\boldsymbol{U},p)$ which is determined by solving the following system of equations:

$$\begin{cases} \mathcal{H}(\boldsymbol{U}, \boldsymbol{U}_a) + \nabla p_a = -\dfrac{K_{\text{crit}}}{K_{\text{BC}}}(1-\tau)C_a\nabla C & \text{in } \Omega & \text{(26a)} \\ \nabla \cdot \boldsymbol{U_a} = 0 & \text{in } \Omega & \text{(26b)} \\ \boldsymbol{U_a} = 0 & \text{on } \Gamma_{\text{in}} \cup \Gamma_{\text{lat}} \cup \Gamma & \text{(26c)} \\ \sigma(\boldsymbol{U_a}, p_a)\boldsymbol{n} + (\boldsymbol{U}\cdot\boldsymbol{n})\boldsymbol{U_a} = 4\nu\tau\varepsilon(\boldsymbol{U})\boldsymbol{n} & \text{on } \Gamma_{\text{out}} & \text{(26d)} \end{cases}$$

with $\mathcal{H}(\boldsymbol{U}, \boldsymbol{U}_a) = -\nu\Delta\boldsymbol{U}_a + (\nabla\boldsymbol{U})^T\boldsymbol{U_a} - \nabla\boldsymbol{U_a}\boldsymbol{U} + \tau 2\nu\Delta\boldsymbol{U}$ and C_a is the adjoint state to C defined as the solution of the following system of equations:

$$\begin{cases} -\mathcal{D}\Delta C_a - \boldsymbol{U}\cdot\nabla C_a + kC_a = 0 & \text{in } \Omega & \text{(27a)} \\ C_a = 0 & \text{on } \Gamma_{\text{in}} & \text{(27b)} \\ \dfrac{\partial C_a}{\partial \boldsymbol{n}} = 0 & \text{on } \Gamma_{\text{lat}} \cup \Gamma & \text{(27c)} \\ C_a(\boldsymbol{U}\cdot\boldsymbol{n}) + \mathcal{D}\dfrac{\partial C_a}{\partial \boldsymbol{n}} = K_{\text{BC}} & \text{on } \Gamma_{\text{out}} & \text{(27d)} \end{cases}$$

In order to ensure the same order of magnitude of C and C_a, the parameter K_{BC} is set to 3×10^{-3} mol.m^{-2}.s^{-1}.

A.3 Catalytic surface reaction case (SR case)

For this case study, a similar reasoning , also detailed by Courtais (2021), is adopted and leads to the following the shape gradient functional:

$$G(\Omega, \lambda_{\mathcal{V}}, \lambda_{\mathcal{E}}) = 2\nu(\varepsilon(\boldsymbol{U}) : \varepsilon(\boldsymbol{U_a}) - \tau\varepsilon(\boldsymbol{U}) : \varepsilon(\boldsymbol{U})) + \frac{K_{\text{crit}}}{K_{\text{BC}}}(1-\tau)\mathcal{D}\frac{\partial C_a}{\partial \boldsymbol{n}}\frac{\partial C}{\partial \boldsymbol{n}} + \lambda_{\mathcal{V}}, \tag{28}$$

where $\boldsymbol{U_a}$ is the solution of Eqs. (26) and C_a is obtained from the following system of equations:

$$\begin{cases} -\mathcal{D}\Delta C_a - \boldsymbol{U}\cdot\nabla C_a = 0 & \text{in } \Omega \quad (29a) \\ C_a = 0 & \text{on } \Gamma_{\text{in}} \cup \Gamma_{\text{lat}} \cup \Gamma \quad (29b) \\ C_a(\boldsymbol{U}\cdot\boldsymbol{n}) + \mathcal{D}\dfrac{\partial C_a}{\partial \boldsymbol{n}} = K_{\text{BC}} & \text{on } \Gamma_{\text{out}} \quad (29c) \end{cases}$$

References

G. Allaire, F. Jouve, and G. Michailidis, 2016. Thickness control in structural optimization via a level set method. *Structural and Multidisciplinary Optimization*, 53(6), 1349–1382, http://dx.doi.org/10.1007/s00158-016-1453-y.

G. Allaire, C. Dapogny, R. Estevez, A. Faure, and G. Michailidis, 2017. Structural optimization under overhang constraints imposed by additive manufacturing technologies. *Journal of Computational Physics*, 351, 295–328, http://dx.doi.org/10.1016/j.jcp.2017.09.041.

G. Allaire and M. Schoenauer, 2007. *Conception optimale de structures*, 58. Springer-Verlag, Berlin, ISBN : 978-3-540-36710-9, http://dx.doi.org/10.1007/978-3-540-36856-4.

D. Attali, 1995. *Squelettes et graphes de Voronoï 2D et 3D*. PhD thesis, Université Joseph Fourier - Grenoble I.

C. Barlier, 1991. Procédé pour la création et la réalisation de pièces par cao et pièces ainsi obtenues. FR Patent FR2673302A1.

B. Benyahia, M. A. Latifi, C. Fonteix, and F. Pla, 2011. Multicriteria dynamic optimization of an emulsion copolymerization reactor. *Computers and Chemical Engineering*, 35(12), 2886–2895, http://dx.doi.org/10.1016/j.compchemeng.2011.05.014.

N. Bianco, M. Iasiello, G. M. Mauro, and L. Pagano, 2021. Multi-objective optimization of finned metal foam heat sinks: Tradeoff between heat transfer and pressure drop. *Applied Thermal Engineering*, 182, 116058, http://dx.doi.org/0.1016/j.applthermaleng.2020.116058.

M. Bonnivard, F. Omnès, and Y. Privat, 2018. Modeling and optimization of hourglass-shaped aquaporins. *Math. Models Methods Appl. Sci.*, 28(8), 1529–1564, http://dx.doi.org/10.1142/S0218202518500422.

J. Bremer, K. H. Rätze, and K. Sundmacher, 2017. Co2 methanation: Optimal start-up control of a fixed-bed reactor for power-to-gas applications. *AIChE Journal*, 63(1), 23–31, http://dx.doi.org/10.1002/aic.15496.

Y. Collette and P. Siarry, 2004. *Multiobjective optimization: principles and case studies*. Springer Science & Business Media, ISBN : 978-3-662-08883-8.

A. Courtais, 2021. *Conceptions optimales de réacteurs à lit fixe par fabrication additive.* PhD thesis, Université de Lorraine.

A. Courtais, A. M. Latifi, F. Lesage, and Y. Privat, 2021a. Shape optimization of fixed-bed reactors in process engineering. *Accepted in SIAM Journal of Applied Mathematics.*

A. Courtais, F. Lesage, Y. Privat, C. Pelaingre, and A. M. Latifi, 2021b. Optimal conception of fixed-bed reactors by stratoconception process using geometry optimization. *Submitted to Computers and Chemical Engineering.*

J.-C. Culioli, 2012. *Introduction à l'optimisation.* Ellipses, ISBN : 978-2-72987-624-1.

C. Dapogny, P. Frey, F. Omnès, and Y. Privat, 2018. Geometrical shape optimization in fluid mechanics using FreeFem++. *Struct. Multidiscip. Optim.*, 58(6), 2761–2788, http://dx.doi.org/10.1007/s00158-018-2023-2.

B. Delmon, P. Grange, and G. Froment, 1997. *Hydrotreatment and hydrocracking of oil fractions.* Elsevier, ISBN : 978-0-08053-426-8.

F. Feppon, G. Allaire, and C. Dapogny, 2020. A variational formulation for computing shape derivatives of geometric constraints along rays. *ESAIM: Mathematical Modelling and Numerical Analysis*, 54(1), 181–228, http://dx.doi.org/10.1051/m2an/2019056.

F. Feppon, G. Allaire, C. Dapogny, and P. Jolivet, 2021. Body-fitted topology optimization of 2d and 3d fluid-to-fluid heat exchangers. *Computer Methods in Applied Mechanics and Engineering*, 376, 113638, http://dx.doi.org/10.1016/j.cma.2020.113638.

J. D. Fonseca, A. M. Latifi, A. Orjuela, G. Rodríguez, and I. D. Gil, 2020. Modeling, analysis and multi-objective optimization of an industrial batch process for the production of tributyl citrate. *Computers and Chemical Engineering*, 132, 106603, http://dx.doi.org/10.1016/j.compchemeng.2019.106603.

I. P. R. Grundtvig, A. E. Daugaard, J. M. Woodley, K. V. Gernaey, and U. Krühne, 2017. Shape optimization as a tool to design biocatalytic microreactors. *Chemical Engineering Journal*, 322, 215–223, http://dx.doi.org/10.1016/j.cej.2017.03.045.

Y. Hadad, S. Rangararajan, K. Nemati, B. Ramakrishnann, R. Pejman, P. R. Chiarot, and B. Sammakia, 2020. Performance analysis and shape optimization of a water-cooled impingement micro-channel heat sink including manifolds. *International Journal of Thermal Sciences*, 148, 106145, http://dx.doi.org/10.1016/j.ijthermalsci.2019.106145.

A. Henrot and M. Pierre, 2005. *Variation et optimisation de forme*, 48. Springer-Verlag, Berlin, http://dx.doi.org/10.1007/3-540-37689-5.

A. Henrot and Y. Privat, 2010. What is the optimal shape of a pipe? *Archive for Rational Mechanics and Analysis*, 196(1), 281–302, http://dx.doi.org/10.1007/s00205-009-0243-8.

A. Hjørungnes, 2011. *Complex-valued matrix derivatives: with applications in signal processing and communications.* Cambridge University Press, ISBN : 978-0-52119-264-4.

G. Holzinger, 2015. OpenFOAM: A little User-Manual. *CD-Laboratory-Particulate Flow Modelling, Johannes Keplper University: Linz, Austria.*

S. Hoseini, G. Najafi, B. Ghobadian, and A. Akbarzadeh, 2020. Impeller shape-optimization of stirred-tank reactor: Cfd and fluid structure interaction analyses. *Chemical Engineering Journal*, 127497, http://dx.doi.org/10.1016/j.cej.2020.127497.

Y. Joo, I. Lee, and S. J. Kim, 2017. Topology optimization of heat sinks in natural convection considering the effect of shape-dependent heat transfer coefficient. *International Journal of Heat and Mass Transfer*, 109, 123–133, http://dx.doi.org/10.1016/j.ijheatmasstransfer.2017.01.099.

S. Kambampati, H. Chung, and H. A. Kim, 2021. A discrete adjoint based level set topology optimization method for stress constraints. *Computer Methods in Applied Mechanics and Engineering*, 377, 113563, http://dx.doi.org/10.1016/j.cma.2020.113563.

R. L. Keeney, H. Raiffa, and D. W. Rajala, 1979. Decisions with multiple objectives: Preferences and value trade-offs. *IEEE Transactions on Systems, Man, and Cybernetics*, 9(7), 403–403, http://dx.doi.org/10.1109/TSMC.1979.4310245.

S. K. Kim and O. Song, 2009. A MAUT approach for selecting a dismantling scenario for the thermal column in KRR-1. *Annals of Nuclear Energy*, 36(2), 145–150, http://dx.doi.org/10.1016/j.anucene.2008.11.034.

O. Levenspiel, 1999. *Chemical reaction engineering.* John Wiley & Sons, ISBN : 978-0-471-25424-9.

E. Logunova and A. Chernyak, 2007. Fixed-bed catalytic reactors for hydrogenation processes. *Chemical & Petroleum Engineering*, 43, http://dx.doi.org/10.1007/s10556-007-0037-5.

J. Mille, A. Leborgne, and L. Tougne, 2019. Euclidean distance-based skeletons: A few notes on average outward flux and ridgeness. *Journal of Mathematical Imaging and Vision*, 61(3), 310–330, http://dx.doi.org/10.1007/s10851-018-0836-7.

D. L. Olson, 1997. Decision aids for selection problems. *Journal of the Operational Research Society*, 48(5), 541–542, http://dx.doi.org/10.1057/palgrave.jors.2600636.

S. Ozguc, L. Pan, and J. A. Weibel, 2021. Topology optimization of microchannel heat sinks using a homogenization approach. *International Journal of Heat and Mass Transfer*, 169, 120896, http://dx.doi.org/10.1016/j.ijheatmasstransfer.2020.120896.

C. Pudney, 1998. Distance-ordered homotopic thinning: a skeletonization algorithm for 3d digital images. *Computer vision and image understanding*, 72(3), 404–413, http://dx.doi.org/10.1006/cviu.1998.0680.

A. Rabhi, A. Chkifa, S. Benjelloun, and A. Latifi, 2018. Surrogate-based modeling in flotation processes. *Computer Aided Chemical Engineering*, 43, 229–234. http://dx.doi.org/10.1016/B978-0-444-64235-6.50041-3.

S. Ramaswami, F. M. J. Uddin, J. Behrendt, and R. Otterpohl, 2019. High-rate nitrification of saline wastewaters using fixed-bed reactors. *Journal of environmental management*, 243, 444–452, http://dx.doi.org/10.1016/j.jenvman.2019.05.020.

Y. Sun, L. Xu, J. Yang, and T. C. Lueth, 2019. Automatic design in matlab using pde toolbox for shape and topology optimization. *ASME International Mechanical Engineering Congress and Exposition*, 59490, V012T10A002. American Society of Mechanical Engineers.

H. K. Versteeg and W. Malalasekera, 2007. *An introduction to computational fluid dynamics: the finite volume method*. Pearson education, ISBN : 978-3-54059-434-5.

J. Villermaux, 1993. *Génie de la réaction chimique*. Technique et Documentation, ISBN : 978-2-85206-759-2.

P. Voola and A. Vinaya Babu, 2017. Study of aggregation algorithms for aggregating imprecise software requirements' priorities. *European Journal of Operational Research*, 259(3), 1191–1199, http://dx.doi.org/10.1016/j.ejor.2016.11.040.